Supporting Information for Publication

Nanoparticle identification using single particle ICP-ToF-MS acquisition coupled to cluster analysis. From engineered to natural nanoparticle

Mickaël Tharaud[§*], Lukas Schlatt[£], Phil Shaw[£], Marc F. Benedetti[§]

[§]Université Paris Cité, Institut de physique du globe de Paris, CNRS, F-75005 Paris, France
[£]Nu Instruments, 74 Clywedog Road South, Wrexham, UK

*Corresponding author:
e-mail: tharaud@ipgp.fr
tel.: +33-1-83-95-78-78

List of content

References used in the SI

1. J. Li, N. Menguy, C. Gatel, V. Boureau, E. Snoeck, G. Patriarche, E. Leroy and Y. Pan, *Journal of The Royal Society Interface*, 2015, **12**, 20141288.
2. J. Li, N. Menguy, M.-A. Arrio, P. Sainctavit, A. Juhin, Y. Wang, H. Chen, O. Bunau, E. Otero, P. Ohresser and Y. Pan, *Journal of The Royal Society Interface*, 2016, **13**, 20160355.
3. S. Lee, X. Bi, R. B. Reed, J. F. Ranville, P. Herckes and P. Westerhoff, *Environmental science & technology*, 2014, **48**, 10291-10300.
4. A. R. Donovan, C. D. Adams, Y. Ma, C. Stephan, T. Eichholz and H. Shi, *Chemosphere*, 2016, **144**, 148-153.
5. L. Fréchette-Viens, M. Hadioui and K. J. Wilkinson, *Talanta*, 2017, **163**, 121-126.
6. O. Borovinskaya, B. Hattendorf, M. Tanner, S. Gschwind and D. Günther, *Journal of Analytical Atomic Spectrometry*, 2013, **28**, 226-233.
7. O. Borovinskaya, S. Gschwind, B. Hattendorf, M. Tanner and D. Günther, *Analytical chemistry*, 2014, **86**, 8142-8148.
8. P. Shaw and A. Donard, *Journal of Analytical Atomic Spectrometry*, 2016, **31**, 1234-1242.
9. A. Azimzada, I. Jreije, M. Hadioui, P. Shaw, J. M. Farner and K. J. Wilkinson, *Environmental Science & Technology*, 2021.
10. M. Tharaud, P. Louvat and M. F. Benedetti, *Analytical and Bioanalytical Chemistry*, 2021, **413**, 923-933.
11. A. Rua-Ibarz, E. Bolea-Fernandez, G. Pozo, X. Dominguez-Benetton, F. Vanhaecke and K. Tirez, *Journal of Analytical Atomic Spectrometry*, 2020, **35**, 2023-2032.
12. M. Tharaud, A. P. Gondikas, M. F. Benedetti, F. von der Kammer, T. Hofmann and G. Cornelis, *Journal of Analytical Atomic Spectrometry*, 2017, **32**, 1400-1411.
13. Y. Dan, H. Shi, C. Stephan and X. Liang, *Microchemical Journal*, 2015, **122**, 119-126.
14. M. D. Montaño, B. J. Majestic, Å. K. Jämting, P. Westerhoff and J. F. Ranville, *Analytical chemistry*, 2016, **88**, 4733-4741.

SI-1. Scanning transmission electron microscopy

In order to verify their composition and their structure, scanning transmission electron microscopy (STEM) analyses were performed on the model ENPs. Few µL of the stock suspensions were deposited onto carbon-coated copper TEM grids 24h prior the analysis and let dry in a clean atmosphere. The analyses were done at IMPMC (Paris, France) using a JEOL-2100F microscope operating at 200 kV. It is equipped with a Schottky emission gun, a JEOL X-ray detector with an ultra-thin window allowing the detection of light elements and a scanning TEM (STEM) device. Thanks to the Z-contrast imaging, high angle annular dark field (STEM-HAADF) imaging mode was initially used to highlight the structure of the NPs. Then, the chemical mapping of the NPs was done using X-ray energy dispersive spectroscopy (XEDS) [1, 2]. The aggregation state of the NPs cannot be assumed based on this method as this is a known artefact of this technique

Gold and/or silver NPs

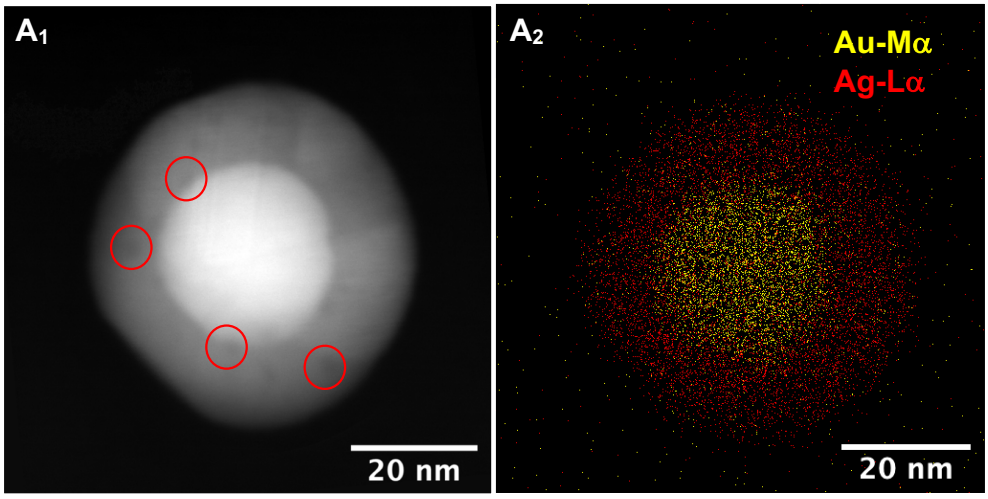

Figure SI-1a: STEM analysis of 60 nm bi-metallic Ag shelled AuNPs (A). Indices 1 and 2 are for STEM-HAADF imaging and STEM-XEDS chemical mapping, respectively. Red arrows point the imperfections (lack of Ag) in the Ag-shell

Scanning transmission electron microscopy (STEM) images of the Ag shelled Au-NPs Figure SI-1a confirm the spherical morphology of the NPs. Moreover, the core-shell structure is verified using HAADF imaging where the contrast allows to distinguish the heaviest element (gold) in the center and the lightest (silver) at the edge of the NP. This is confirmed by the XEDS mapping displaying the bi-metallic "Au-core – Ag-shell" composition. Nevertheless, NPs observed (n = 10) seem to be in the low range of the theoretical size displayed in the certificate (59 ± 6 nm). Additionally, imperfections (*i.e.* lack of Ag) are observed in the Ag-shell as highlighted by the red circles.

Nickel/Zinc Cobalt Iron oxide NPs

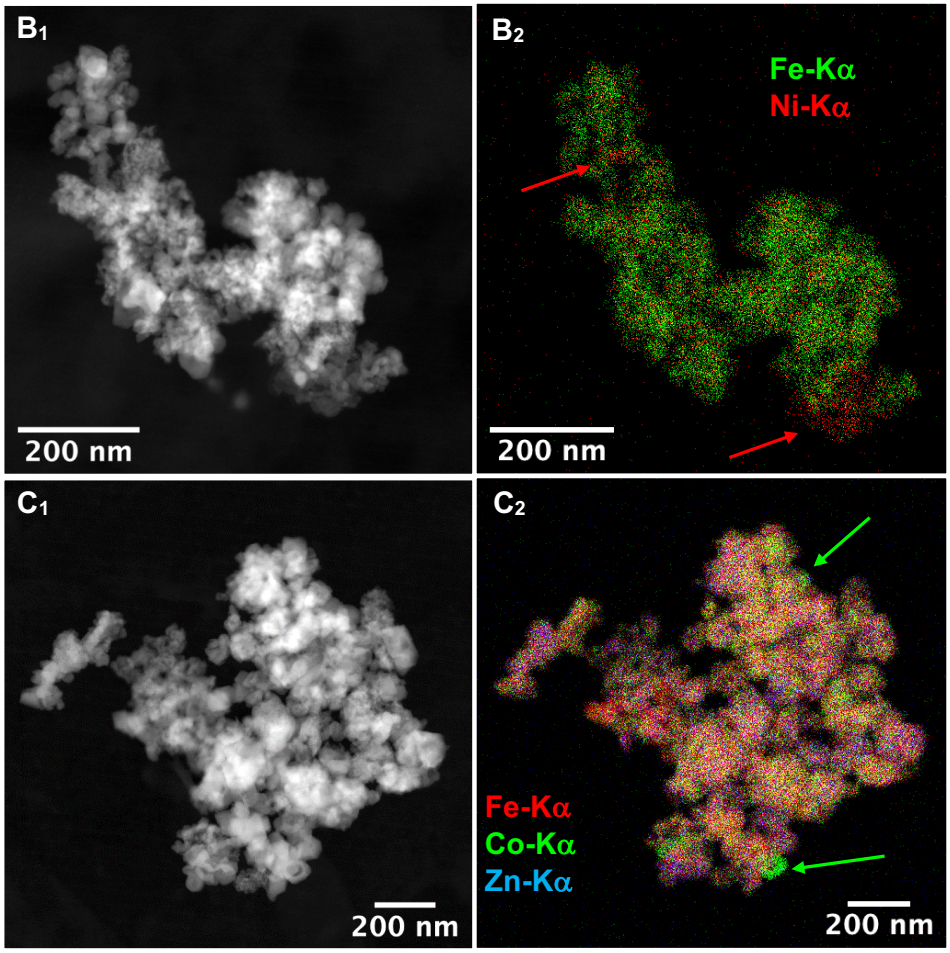

Figure SI-1b: STEM analysis of Nickel Cobalt Iron oxide (B) and Zinc Cobalt Iron oxide (C). Indices 1 and 2 are for STEM-HAADF imaging and STEM-XEDS chemical mapping, respectively. Red and green arrows point hot-spots of Ni and Co, respectively

Figure SI-1b displays the images of scanning transmission electron microscopy (STEM) for Nickel/Zinc Cobalt Iron oxides. The images show no evidence of a core-shell structure and/or of a homogeneous size distribution (40 nm, given in the certificate). Indeed, most of the particles observed are above 350 - 400 nm with a heterogeneous size distribution. However, no information about the size of the NPs and/or aggregation state can be extracted from these images as STEM preparation influences the formation of such amasses. Still, the XEDS mapping demonstrates that elements are heterogeneously distributed in the agglomerate with hot-spots of some elements (*i.e.* Ni and Co in Figure SI-1b B_2 and C_2, respectively).

SI-2. External calibration and size detection limits of the spICP-ToF-MS

Table SI-2: Representative results of the spICP-ToF-MS external calibrations as well as M_{min} and D_{min} in ultrapure water.

Isotope	*sensitivity (cts sec^{-1} L µg^{-1})*	*R^2*	*σ_{UPW} (cts sec^{-1})*	*M_{min} (fg)*	*ρ (g cm^{-3})*	*D_{min} (nm)*
^{24}Mg	4069.5	0.999	2637.4	0.605	1.74	87.2
^{27}Al	11293.6	0.999	7904.1	0.643	2.70	76.9
^{28}Si	3448.7	0.886	10805.4	2.924	2.33	133.8
^{40}Ca	38786.2	0.900	21823.7	0.525	1.55	86.7
^{48}Ti	20330.7	1.000	3079.1	0.148	4.54	39.7
^{56}Fe	35492.9	0.994	7086.6	0.238	7.87	38.7
^{59}Co	48377.6	1.000	1322.5	0.033	8.82	19.2
^{60}Ni	10444.3	0.999	2000.1	0.179	8.90	33.7
^{66}Zn	5465.4	0.999	1442.7	0.246	7.13	40.4
^{107}Ag	14388.6	1.000	1171.6	0.076	10.49	24.0
^{197}Au	16436.0	0.994	2123.7	0.121	19.32	22.8

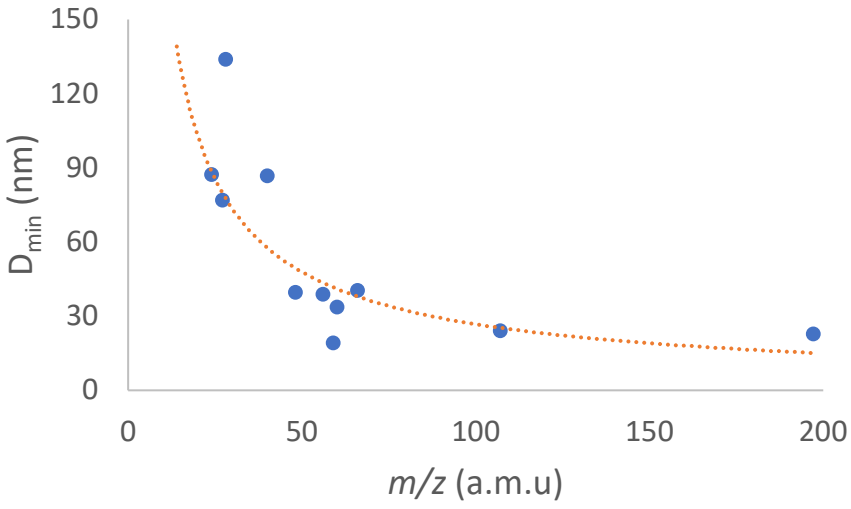

Figure SI-2: Minimum size detectable (D_{min}) vs mass on charge ratio (m/z) using data in Table 3

Table SI-2 displays the results of each individual isotopes external calibration using mono-elemental standards mixed together in 1% HNO_3. The coefficient of determination (R^2) of their individual linear regression fits, calculated using the least square method, show a linear response in the range of 100 – 20000 ng L^{-1}. The minimum detectable mass (M_{min}) and minimum detectable diameter (D_{min}) are listed in Table and D_{min} is also displayed in Figure SI-2 as a function of mass on charge (m/z) ratio. Following previous studies [3] the sensitivity in cts sec^{-1} L µg^{-1} is first converted in cts µg^{-1} using the transport rate (here 0.16 µL sec^{-1}). Then, the standard deviation of the background in cts sec^{-1} as determined by all datapoints in which no particle events were detected is used along with the average

particle duration to determine the M_{min}. Finally, assuming a spherical shape of pure metal, the D_{min} is calculated. D_{min} reported in this study for Au and Ag are in the range of those presented in the literature for quadrupole [4, 5] or time-of-flight [6, 7] based instruments. Much lower D_{min} are usually reported for sector-field based instruments as the sensitivity is much higher [8-10]. For Fe, the resolution of the $^{40}Ar^{16}O$ interference is a key factor ($R \geq 2500$). Although ICP-SF-MS has higher sensitivity, ^{56}Fe is usually measured in medium-resolution mode to fully resolve the interference, which gives a 10-fold lower response and thus slightly higher D_{min}. Rua-Ibarz et *al.* (2020) [11] have shown that the use of high sensitivity instruments such as an ICP-SF-MS in pseudo-medium-resolution mode or an ICP-MS/MS in H_2 mode decreases the D_{min} for Fe_3O_4 (D_{min} = 19 nm; *ca.* 13.7 nm for pure FeNPs). The resolution power of this ICP-ToF-MS (*ca.* 3500 FWHM) combined to a collision cell with H_2 and He (always on) allows the full removal of the $^{40}Ar^{16}O$ interference. The lower sensitivity compared to those reported in the study mentioned above however leads to a higher D_{min}. Polyatomic interferences also need to be resolved for Zn, Ni and Co and the resolution power of the time-of-flight coupled to the collision cell looks efficient as D_{min} are very low compare to the D_{min} reported by Lee et *al.* (2014) [3] for ICP-Q-MS. Zn, Ni and Co natural abundances are respectively 27.97, 26.22 and 100% and the first ionization energies of Zn (*i.e.* 9.39 eV) is much higher than the others (7.64 and 7.88 eV, respectively), leading to the reported sensitivities with $S_{Zn} < S_{Ni} < S_{Co}$. Additionally, as their $3\sigma_{UPW}$ and their densities (used for the calculation of the D_{min}) are quite close, this leads to D_{min} decreasing as followed: Zn > Ni > Co. The case of ^{48}Ti is much complex as there is an isobaric interference (*i.e.* ^{48}Ca) more difficult to resolve. In a previous study [12], we demonstrated that the use of the high-resolution mode (*i.e.* $R \approx 10000$) on an ICP-SF-MS is necessary to reach $D_{min} \approx 10$ nm in presence of high ionic Ca. The absence of ionic Ca here allows to reach low D_{min}, nevertheless this is in the range of those reported for ICP-Q-MS for instance [4, 13]. While D_{min} at $m/z > 40$ are quite low (*i.e.* ≤ 40 nm), an increase is observed at $m/z \leq 40$ (*i.e.* > 70 nm) (Figure SI-2). The D_{min} of ^{24}Mg and ^{27}Al calculated here are however in the range of the one reported in the synthesis of Lee et *al.* (2014) [3]. The high background of Si and Al is probably influenced by the composition of the introduction system entirely made of borosilicate glass that can lead to high D_{min}. Additionally, the highest of all D_{min} displayed for ^{28}Si is also due to its low sensitivity. This D_{min} is however lower than the one reported in other studies [3, 14]. For ^{40}Ca, it is probable that the removal of ^{40}Ar is not 100% efficient. However, the collision cell still looks very powerful as at least 99.5% of ions that are extracted from the plasma are $^{40}Ar^+$ and only few counts are detected at $m/z = 40$.

SI-3. Supplementary figures for model NNPs

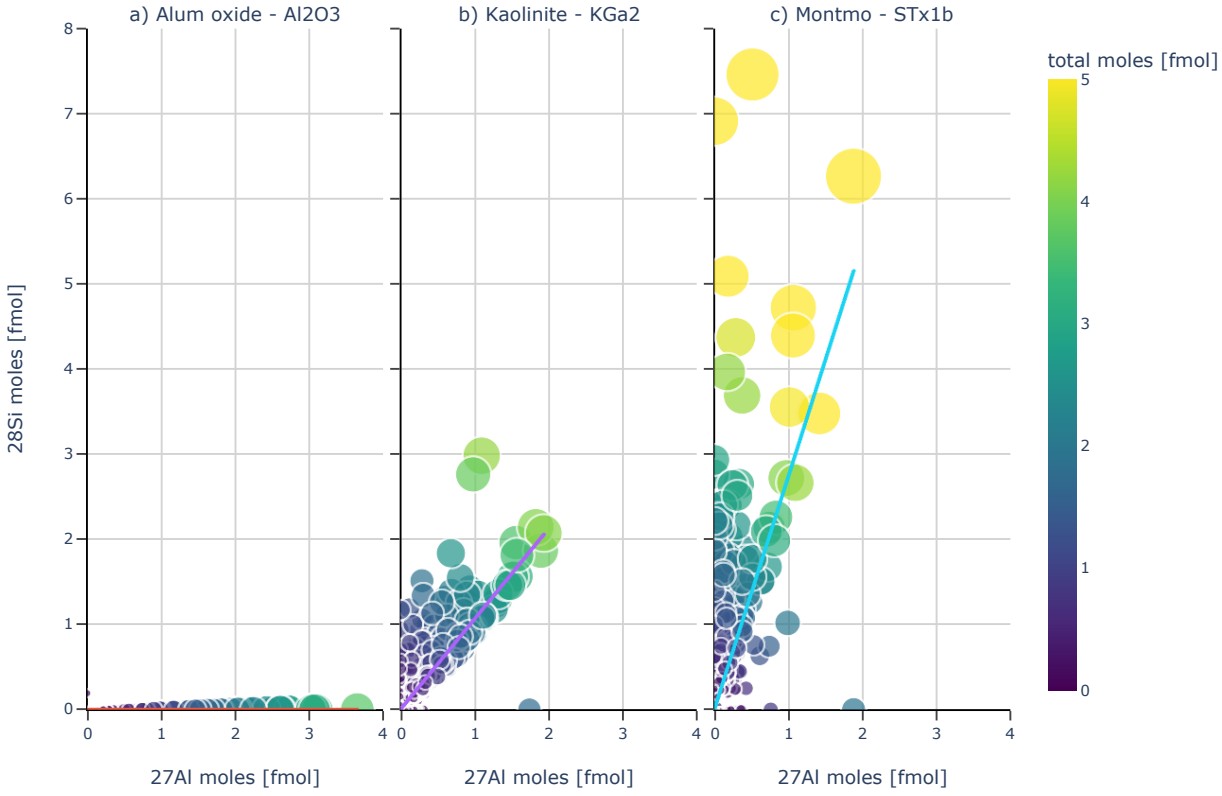

Figure SI-3a: Number of moles of Si vs the number of moles of Al (all in femtomoles). Purple, blue and green lines represent the best fit lines, for KGa-2 and STx-1b, respectively. The color bar gives the total amount of moles (in femtomoles) in individual datapoints while the size of each point is related to the calculated total mass of each NP. Note that the molar fraction, the total amount of moles and the mass are calculated using the sum (mole or mass) of the elements detected within the NP

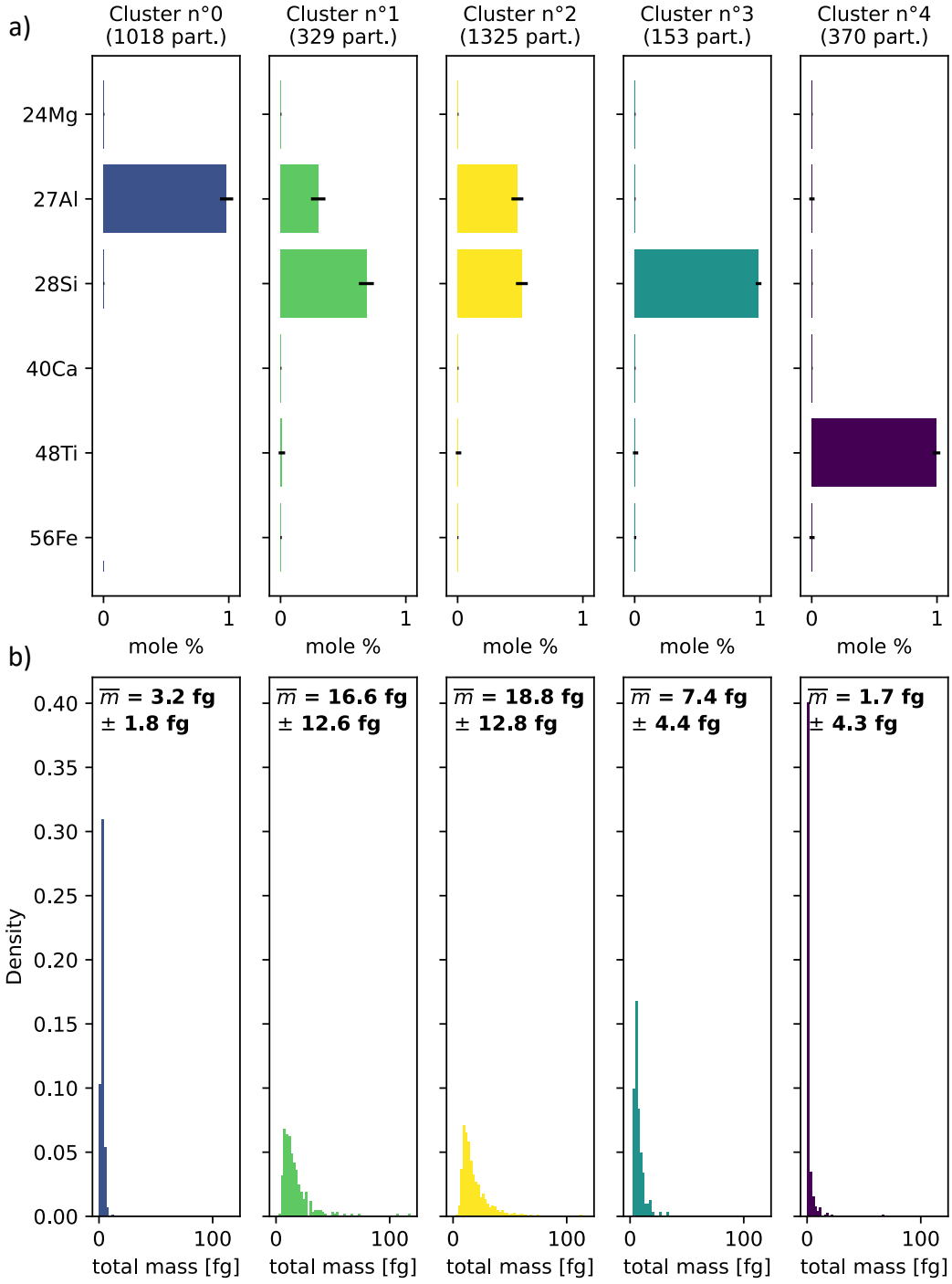

Figure SI-3b: Summary of the hierarchical agglomerative clustering on spICP-ToF-MS data of the kaolinite - KGa-2 - only. a) Molar fractions and b) particle mass distributions of individual clusters are displayed.

SI-4. Supplementary screenshots of spICP-ToF-MS time-based graphic records

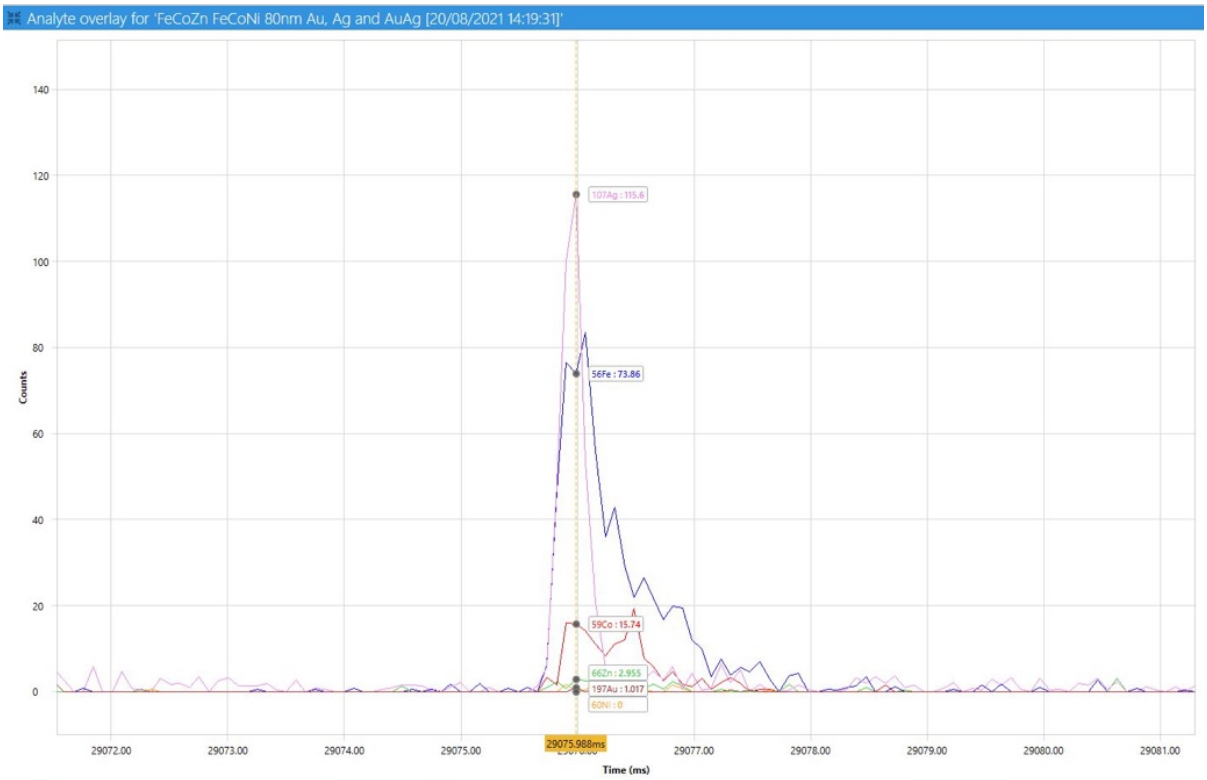

Figure SI-4a: Screenshot of a spICP-ToF-MS time-based graphic records of the multi-NP mixture. Example of a multi-metallic event demonstrating hetero-aggregation within the mixture

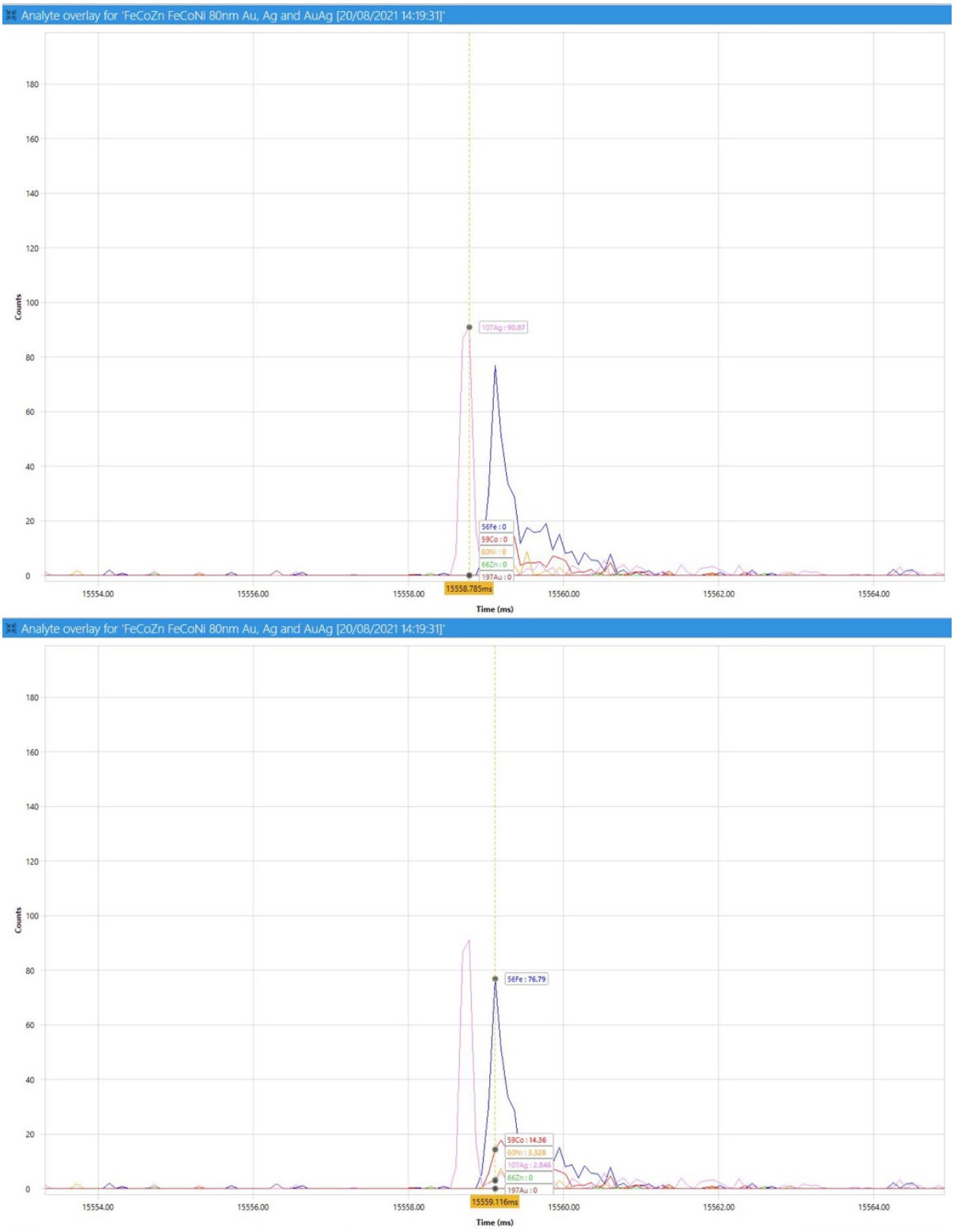

Figure SI-4b: Screenshots of spICP-ToF-MS time-based graphic records of the multi-NP mixture. Examples of a multi-metallic event demonstrating an overlap between pure Ag and Fe-Co-Ni peaks (i.e. coincidence). This leads to consider these two not well separated peaks as a single peak during the data treatment in NuQuant

SI-5. Minimum size detectable of tri-metallic NPs

As displayed in the graphs below, the ability of the ICP-ToF-MS to detect Ni and Zn is first altered while decreasing the total mass of the NP. Indeed, the solid line which represent the total mass of a tri-metallic NP and the dashed line which is the mass of the element in the tri-metallic NP intercept at higher total masses for Ni and Zn compare to Fe and Co. This means that the detection limits of Ni and Zn combine to their low molar ratio in the tri-metallic NPs is the limiting factor for the detection of this particular NPs. This interception is at *ca.* 1.40 and 1.80 fg for Ni and Zn, respectively. Assuming the theoretical molar fraction, this leads to minimum size detectable for $Ni_{0.5}Co_{0.5}Fe_2O_4$ and $Zn_{0.5}Co_{0.5}Fe_2O_4$ of *ca.* 80 and 87 nm, respectively.

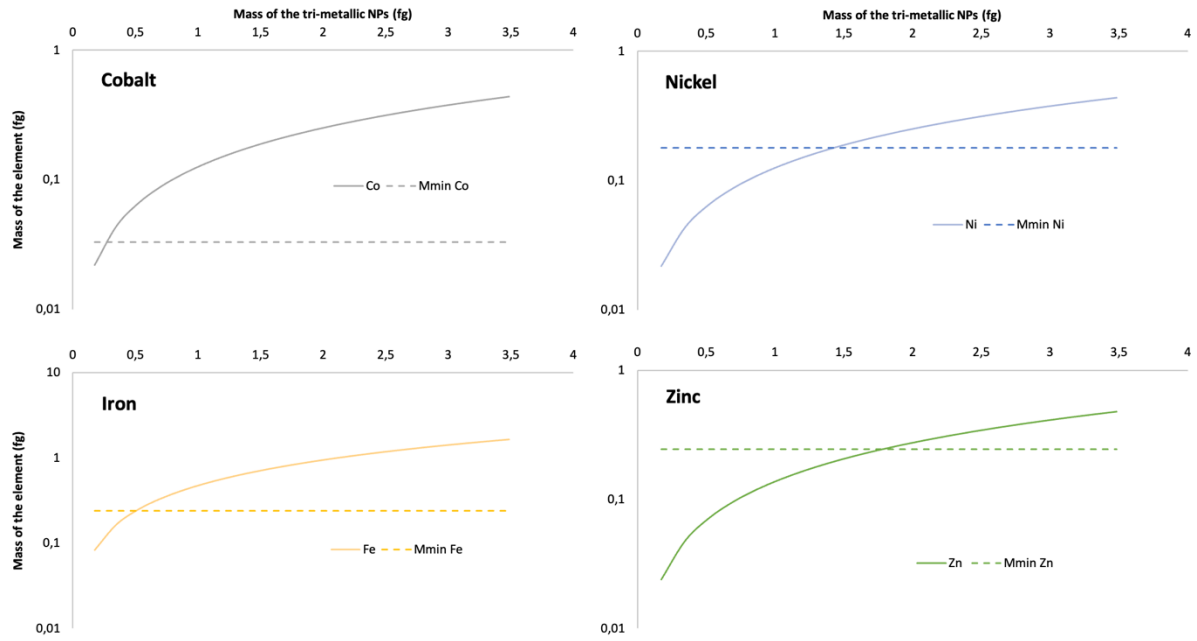

Figure SI-5: Mass (in fg, log-scale) of the element in the NP vs the mass (in fg) of the tri-metallic NP with oxygen (i.e. $Ni_{0.5}Co_{0.5}Fe_2O_4$ and $Zn_{0.5}Co_{0.5}Fe_2O_4$). Solid line represents the mass of the element in the NP calculated with the theoretical molar ratio (including oxygen). The dashed line represents the minimum mass detectable (Mmin) by the ICP-ToF-MS (Table SI-2)